This is a repository copy of *Applying the weighted horizontal magnetic gradient method to a simulated flaring Active Region*.

White Rose Research Online URL for this paper:
http://eprints.whiterose.ac.uk/130725/

Version: Published Version

Article:
Korsos, M.B., Chatterjee, P. and Erdelyi, R. (2018) Applying the weighted horizontal magnetic gradient method to a simulated flaring Active Region. Astrophysical Journal, 857. 103. ISSN 0004-637X,

https://doi.org/10.3847/1538-4357/aab891

Reuse
Items deposited in White Rose Research Online are protected by copyright, with all rights reserved unless indicated otherwise. They may be downloaded and/or printed for private study, or other acts as permitted by national copyright laws. The publisher or other rights holders may allow further reproduction and re-use of the full text version. This is indicated by the licence information on the White Rose Research Online record for the item.

Takedown
If you consider content in White Rose Research Online to be in breach of UK law, please notify us by emailing eprints@whiterose.ac.uk including the URL of the record and the reason for the withdrawal request.

eprints@whiterose.ac.uk
https://eprints.whiterose.ac.uk/

The Astrophysical Journal, 857:103 (12pp), 2018 April 20 https://doi.org/10.3847/1538-4357/aab891
© 2018. The American Astronomical Society. All rights reserved.

Applying the Weighted Horizontal Magnetic Gradient Method to a Simulated Flaring Active Region

M. B. Korsós[1,2,3], P. Chatterjee[4], and R. Erdélyi[1,3]
[1] Solar Physics & Space Plasma Research Center (SP2RC), School of Mathematics and Statistics, University of Sheffield, Hounsfield Road, S3 7RH, UK
korsos.marianna@csfk.mta.hu
[2] Debrecen Heliophysical Observatory (DHO), Research Centre for Astronomy and Earth Sciences, Hungarian Academy of Science, 4010 Debrecen, P.O. Box 30, Hungary
[3] Department of Astronomy, Eötvös Lóránd University, Pázmány Péter sétány 1/A, Budapest, H-1117, Hungary; robertus@sheffield.ac.uk
[4] Indian Institute of Astrophysics, II Block Koramangala, Bengaluru-560034, India; piyali.chatterjee@iiap.res.in
Received 2017 March 29; revised 2018 March 19; accepted 2018 March 19; published 2018 April 20

Abstract

Here, we test the weighted horizontal magnetic gradient (WG_M) as a flare precursor, introduced by Korsós et al., by applying it to a magnetohydrodynamic (MHD) simulation of solar-like flares. The preflare evolution of the WG_M and the behavior of the distance parameter between the area-weighted barycenters of opposite-polarity sunspots at various heights is investigated in the simulated δ-type sunspot. Four flares emanated from this sunspot. We found the optimum heights above the photosphere where the flare precursors of the WG_M method are identifiable prior to each flare. These optimum heights agree reasonably well with the heights of the occurrence of flares identified from the analysis of their thermal and ohmic heating signatures in the simulation. We also estimated the expected time of the flare onsets from the duration of the approaching–receding motion of the barycenters of opposite polarities before each single flare. The estimated onset time and the actual time of occurrence of each flare are in good agreement at the corresponding optimum heights. This numerical experiment further supports the use of flare precursors based on the WG_M method.

Key words: Sun: evolution – Sun: flares – sunspots

Supporting material: animations

1. Introduction

Solar active regions (ARs) are among the most investigated dynamic features on the Sun that are identified as a collection of strong positive and negative magnetic polarity elements (sunspots) in magnetograms. A sunspot is classified as δ-type when the opposite magnetic polarities share a common penumbra (Künzel 1960). The magnetically complicated and highly dynamic δ-type sunspot groups are more likely to produce flares and coronal mass ejections (CMEs) than the bipolar ones (Guo et. al. 2006; Sammis et al. 2000). Studying the δ-type sunspot groups may be a key element to reveal the characteristic temporal variations of the evolution of the magnetic field prior to flares (Leka et al. 1996; van Driel-Gesztelyi et al. 1997; Takizawa & Kitai 2015).

In the literature, several studies have addressed the spatial and temporal evolution of the flare-triggering phenomena. Observational and numerical investigations report that newly emerged magnetic flux (Archontis & Hood 2008; MacTaggart & Hood 2009), flux cancellation (Livi et al. 1989; Wang & Shi 1993; Sterling et al. 2010; Green et al. 2011; Savcheva et al. 2012; Burtseva & Petrie 2013), strong magnetic shear, and the rotation (Evershed 1910; Kempf 1910; Manchester & Low 2000; Manchester et al. 2004; DeVore & Antiochos 2008; Yan et al. 2008; Selwa et al. 2012) along the polarity inversion line (PIL), the length or strong horizontal gradient across the PIL (Schrijver 2007; Falconer et al. 2008) all seem to be, with various degrees, candidates for flare and CME triggers. Also, a range of flare and CME models exists where the complex configuration of an AR is proposed to lead to solar eruptions (Aschwanden 2005; Li et al. 2005; Shibata & Magara 2011, and references therein).

Here, we investigate the evolution of the opposite magnetic polarities in a 3D numerical model of a δ-type sunspot. We test the concept of the weighted horizontal magnetic gradient (WG_M) method proposed by Korsós et al. (2015, hereafter K15) by analyzing the emerging magnetic flux that generates a series of flares in the simulation, first reported in Chatterjee et al. (2016). In Section 2, we briefly outline the simulation setup and the numerical code used. In Section 3, we perform a detailed analysis of the flaring regions of the simulation in terms of ohmic heating and temperature increase for comparison of the findings with the WG_M method given in Section 4. We describe the WG_M method itself and present our analysis of the simulated AR, followed by summarizing our findings. Finally, we discuss our results and draw conclusions in Section 5.

2. The MHD Model

Our analysis is centered on the numerical case study reported in Chatterjee et al. (2016). For completeness, we briefly describe the salient points of the model setup here. The computational domain consists of a box with horizontal extents of -18 Mm $< x, y <$ 18 Mm and a vertical one of -8.5 Mm $< z <$ 16.5 Mm, rotating with a solar-like angular velocity $\Omega = 2.59 \times 10^{-6}\,\mathrm{s}^{-1}$, making an angle of 30° with the vertical z-direction. A constant gravity, g_z, points in the negative z-direction. The box is resolved using a uniformly spaced grid with $dx = dy = 96$ km and $dz = 48$ km. The box may be thought to be placed at a colatitude θ on the surface of a sphere with its unit vectors, $\hat{\boldsymbol{x}}$, $\hat{\boldsymbol{y}}$, and $\hat{\boldsymbol{z}}$, pointing along the local ϕ, $-\theta$, and r directions, respectively, as shown in Figure 1(a). We use the fully compressible higher-order finite difference

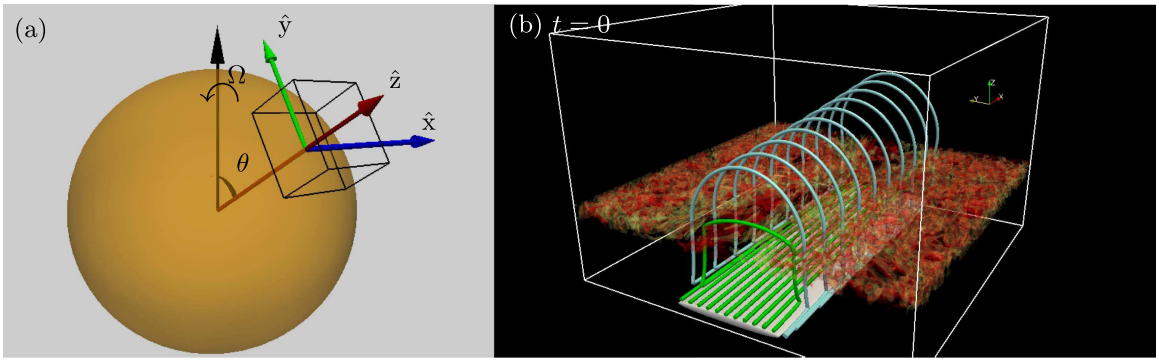

Figure 1. (a) Cartesian simulation domain with respect to spherical coordinates. For visual clarity, the ratio of the horizontal extent of the box to the radius of the sphere in the picture is 10 times larger than that used in the simulation. (b) Initial state inside the box with a thin magnetic layer represented by the isosurface of $B\rho^{-1/4}$ (white). A few field lines in this layer are shown in green. Additionally, the ambient (arcade-shaped) magnetic field lines are shown in cyan. The location of the photosphere is marked by convective granules represented by isosurfaces of v_z, with red (yellow) representing upward (downward) v_z.

tool, the PENCIL CODE[5], for these calculations. This code is highly modular and can easily be adapted to different types of computational MHD problems.

The induction equation is solved for the magnetic vector potential, $\boldsymbol{A}$, using the uncurled induction equation

$$\frac{\partial \boldsymbol{A}}{\partial t} = \boldsymbol{U} \times \boldsymbol{B} - \eta \boldsymbol{J} + \nabla \Psi, \tag{1}$$

where $\nabla \times \boldsymbol{A} = \boldsymbol{B}$ and η denotes molecular magnetic diffusivity. Gauge freedom allows us to set $\Psi = 0$ (Weyl gauge) at all times. The initial expression for the components of $\boldsymbol{A}$, corresponding to a horizontal magnetic sheet at $z_0 = -7.75$ Mm (shown by the white isosurface in Figure 1(b)) with the magnetic field vector, $\boldsymbol{B}$, strongly oriented in the x-direction, are given by

$$A_x = q\varpi\Phi;\ A_y = -(z - z_0)\Phi;\ A_z = y\Phi,$$

where $\Phi = B_0 R^2[1 - \exp\{-\varpi^2/R^2\}]/\varpi$ with $B_0 = 50$ kG, $\varpi^2 = (a\,y)^2 + (z\text{–}z_0)^2$, and $a = 0.1$. The horizontal extent of the sheet is about $-3\,\mathrm{Mm} < y < 3\,\mathrm{Mm}$, and the maximum half-width, R, is 0.3 Mm at $\boldsymbol{y} = 0$. With this value of R, the twist parameter, q, is thus 0.1, corresponding to an initially weak negative twist. We also introduce an ambient magnetic field in the form of a potential field arcade at $z > 0$, also shown in Figure 1(b). The lower boundary at $z = -8.5$ Mm is closed, and the top boundary at $z = 16.5$ Mm is open. The x-boundaries are periodic, whereas the y-boundaries are perfectly conducting walls. Finally, we have for the entropy equation with temperature T, height-dependent thermal conductivity K, and turbulent diffusion χ_t,

$$\rho T \frac{Ds}{Dt} = \boldsymbol{\nabla} \cdot (K \nabla T) + \boldsymbol{\nabla} \cdot (\rho T \chi_t \nabla s) + \eta \mu_0 \boldsymbol{J}^2 + 2\rho\nu \mathsf{S}^2 - \rho^2 \Lambda(T) + Q_{\mathrm{Cor}}, \tag{2}$$

where the temperature is related to the sound speed by $c_s^2 = (c_p - c_v)\gamma T$. The last two terms in Equation (2) are the radiative cooling and coronal heating terms, respectively.

We include explicit height-dependent viscosity in the velocity equation, $\nu/\nu_0 = 1 + f(1 + \tanh\{(z - z_1)/w\})$, whereas magnetic diffusivity, η/η_0, and isotropic thermal conductivity, K/K_0, vary as $(\rho_{\mathrm{in}}/\rho_0)^{-1/2}$, with $f = 150$, $z_1 = 2$ Mm, $w = 1.5$ Mm, $\nu_0 = 2 \times 10^{10}\,\mathrm{cm^2\,s^{-1}}$, $\eta_0 = 10^4\,\mathrm{cm^2\,s^{-1}}$, $K_0 = 5 \times 10^4\,\mathrm{cm^2\,s^{-1}}$, and ρ_{in} as the initial density. The turbulent diffusion $\chi_t = 10^{11}\,\mathrm{cm^2\,s^{-1}}$ for $z < 0$ and tends to zero above that. Additionally, we use hyper-dissipation and shock viscosity proportional to positive flow convergence, maximum over three zones, and smoothed to second order. A density diffusion of $10^{11}\,\mathrm{cm^2\,s^{-1}}$ is also included throughout, since the plasma-β reaches values of $\sim 10^{-3}$. After a time, $t = 220$ minutes in the simulation, we have increased the value of the density diffusion to $10^{12}\,\mathrm{cm^2\,s^{-1}}$ and $f = 300$ to prevent the velocities from going to infinity in the code.

[5] https://github.com/pencil-code/

Table 1
Summary of the Energy Released, Onset Times, Durations, and Estimated Occurrence Heights for the Four Flares

	B_1	C_1	B_2	C_2
$\delta\mathcal{E}_B$ (10^{29} erg)	3.3	17.0	2.0	23.0
Onset time (minutes)	167.5	197.2	215.03	240.2
Duration (minutes)	5.0	25.0	13.0	>23.0
Height range (Mm):				
$\Delta T/\bar{T}(z)$	>0.6	<3.24	<1.28	⩽3.24
Peak of Q_{FL}	0.4–1.5	2.5	0.3–0.5	3.0
WG_M	0.3–0.4	2.3–2.9	0.5	1.2–1.8

3. Analysis of Temperature and Ohmic Heating in the Simulation

The simulation was run for 263 minutes of solar time starting from the initial state shown in Figure 1(b). It takes about 145 minutes from the start for the initial magnetic sheet to break up, rise, and emerge through the surface like a newly emerging AR. Afterward, there were four eruptions identified as flares (B_1, C_1, B_2, and C_2) with magnetic energy released equal to 3.3×10^{29}, 1.7×10^{30}, 2×10^{29}, and 2.3×10^{30} erg at simulation onset times $t = 167.5$ (B_1), $t = 197.2$ (C_1), $t = 215.03$ (B_2), and $t = 240.2$ minutes (C_2), respectively. Comparing with the estimates made by Isobe et al. (2005) for a C-class flare that occurred on 2000 November 16, we conclude that the first and third flares can be categorized as *Geostationary Operational Environment Satellites* (*GOES*) B-class, whereas the second and fourth can be categorized as *GOES* C-class for the amount of X-ray flux emitted. In Table 1, we show the onset times, energy released, and estimated reconnection height for each flare. The onset times of the

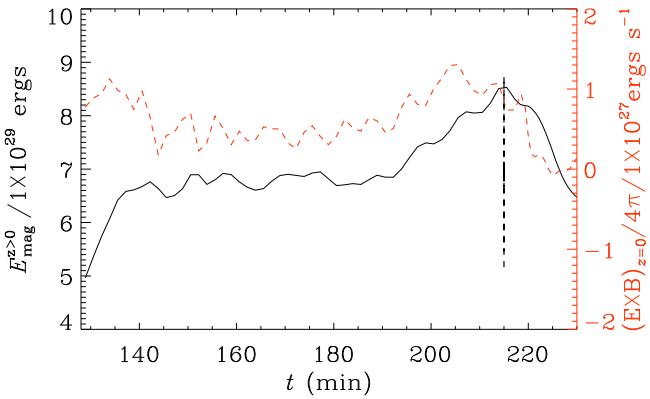

Figure 2. Evolution of magnetic energy (black line) and Poynting flux (red line) over an area surrounding the B_2 flare. The dashed vertical line denotes $t = 215.03$ minutes, the onset time of the flare.

flares are obtained from the temporal evolution of the magnetic energy. For example, Figure 2 shows the evolution of magnetic energy (black) and the Poynting flux (red) in a subdomain surrounding the B_2 flare. The flare onset for this flare occurs at $t = 215.03$ minutes when there is a local maximum in the energy curve and the slope of the energy curve starts to change sign from positive to negative, with the energy decreasing rapidly. In order to differentiate the flare onset signal from other fluctuations, we combine the information on change of slope of energy versus time with the first appearance of the flashes of high temperature in the accompanying animation files at three different heights. Also, we use the information from the time of occurrence of the bipolar reconnection jets in Figure 4(b) of Chatterjee et al. (2016) for the B_1, C_1, and C_2 flares, which matches with the time from the energy curves in Figure 4(a) of the same paper. The magnetic energy, $\delta\mathcal{E}_B$, released during the B_2 flare is calculated to be 2×10^{29} erg. The $\delta\mathcal{E}_B$ values for the B_1 and C_1 flares were given in Chatterjee et al. (2016), as well as in Table 1 for completeness. The Poynting flux into the area surrounding the flare also decreases rapidly after $t = 215.03$ minutes and becomes close to zero.

In Figure 3, we show the contours of the temperature anomaly as ΔT relative to the horizontal average, denoted $\overline{T}(z)$, at three different heights: $z = 0.59$, 1.28, and 3.24 Mm for all of the flares we study in the simulation. A positive (negative) ΔT implies that the local temperature is greater (less) than $\overline{T}(z)$ of the horizontal layer. It is clear from the temperature indicator that the B_2 flare occurred much below $z = 3.24$ Mm, whereas some signatures of the B_1 and C_1 flare can still be detected at this height. Moreover, the B_2, C_1, and C_2 flares can be detected much lower in the atmosphere, e.g., as low as $z = 0.59$ Mm, contrary to B_1, which does not show any brightening at this height at $t = 168.89$ minutes. However, from a later time, $t = 170.56$ minutes, we start seeing the flare brightening for B_1 at the height $z = 0.59$ Mm (see the accompanying animation file 0p55MmFlares.mp4 after $t = 167$ minutes in the online journal). This means that the reconnection for flare B_1 was actually initiated higher up, and it took ~2 minutes for the reconnection current sheet to stretch downward, thus increasing the temperature of the lower layers. Similarly, from the animation 1p28MmFlares.mp4 (again, see online material), after $t = 167$ minutes, one can also spot the reconnection jet before the appearance of the bright inverse-shaped flux rope. This may mean that reconnection for the B_1 flare was actually initiated somewhere between 0.59 and 1.28 Mm. Also note that the B_1 and B_2 flares erupted over different regions of the simulation domain. In general, all flares appear bright in terms of $\Delta T/\overline{T}(z)$ at $z = 1.28$ Mm. The last flare, C_2, is most likely a filament eruption, as evident from two neighboring inverse-S-shaped dark filamentary structures in the $\Delta T/\overline{T}(z)$ contour plot at all heights. The evolution and eruption of this filament-like structure are shown in Figure 6 of Chatterjee et al. (2016). There one sees some smaller bright regions surrounding the dark filaments at the heights $z = 0.59$ and 1.28 Mm. A corresponding bright region at $z = 3.28$ Mm is not so prominent, likely because of a large coronal conductivity used in the MHD equations after $t = 220$ minutes.

A simulation snapshot at $t = 198.8$ minutes showing the reconnection jet along the reconnecting field lines during the occurrence of the C_1 flare is shown in Figure 4. One important feature of the simulation seen in this figure is the self-consistent formation of helical and buoyant magnetic flux tubes under the action of magnetic buoyancy instability on a thin magnetic sheet in the presence of rotation and stratification. Furthermore, the flux tubes formed are nonuniformly twisted along their length and therefore can emerge out of the photosphere only at certain points where the twist is large. This alleviates the need to use uniformly twisted flux tubes with twist as a free initial parameter. We will describe our detailed analysis of flare initiation sites later in the text.

We have used ideal gas thermodynamics in this simulation without solving for detailed radiative transfer or taking into account the effects of ionization. Also, in order to keep the simulation stable at low plasma-β, we have used higher dissipation. All of these approximations can make the temperature in the simulation a less reliable indicator. Alternatively, we can also estimate the ohmic heating of field lines above the photospheric height in the simulation using a method similar to the one illustrated in Cheung & DeRosa (2012). The ohmic heating term in Equation (2) is given by $\eta\mu_0\boldsymbol{J}^2$. If, however, we were to write an equation for the temperature, T, instead of for entropy, s, the ohmic heating term would be given by $\eta\mu_0\boldsymbol{J}^2/\rho C_v$. Assuming that the thermal conductivity along the magnetic field lines far exceeds the isotropic thermal conductivity in the solar corona, we can assign a quantity, $\tau_{\mathcal{L}}$, to a line-tied field line, $\mathcal{L}$, where

$$\tau_{\mathcal{F}} = \frac{\mu_0}{c_v \mathcal{L}} \int_{\mathcal{F}} \frac{\eta \boldsymbol{J}^2}{\rho} d\boldsymbol{l}.$$

Here, c_v is the specific heat capacity at constant volume and $d\boldsymbol{l}$ is an infinitesimal distance along the field line $\mathcal{F}$ of length $\mathcal{L}$ between the line-tied ends at the photosphere. We trace about 10^5 field lines through all points on the photosphere where $B_z > 200$ G and assign a unique $\tau_{\mathcal{F}}$ to all field lines. If the field line crosses any of the side boundaries or the top boundary, we set $\tau_{\mathcal{F}} = 0$ for that field line. Now any magnetic field line will traverse through many grid cells in the computational domain. For each grid cell, we define the increment in the value of ohmic heating denoted, $Q_{\rm FL}(x, y, z)$, by

$$dQ_{\rm FL} = \tau_{\mathcal{F}} dxdy.$$

Hence, the net heating due to field lines, $Q_{\rm FL}$, for any grid cell will be the sum of $\tau_{\mathcal{F}}$ for all field lines passing through that cell. A region like a current sheet or flux rope will appear bright in $Q_{\rm FL}$, as all field lines passing through it carry large currents and so have a large value of $\tau_{\mathcal{F}}$. The three-dimensional ohmic heating, $Q_{\rm FL}(x, y, z)$, at the onset time of all four flares—B_1, C_1, B_2, and C_2—as viewed from the z-direction is shown in the left

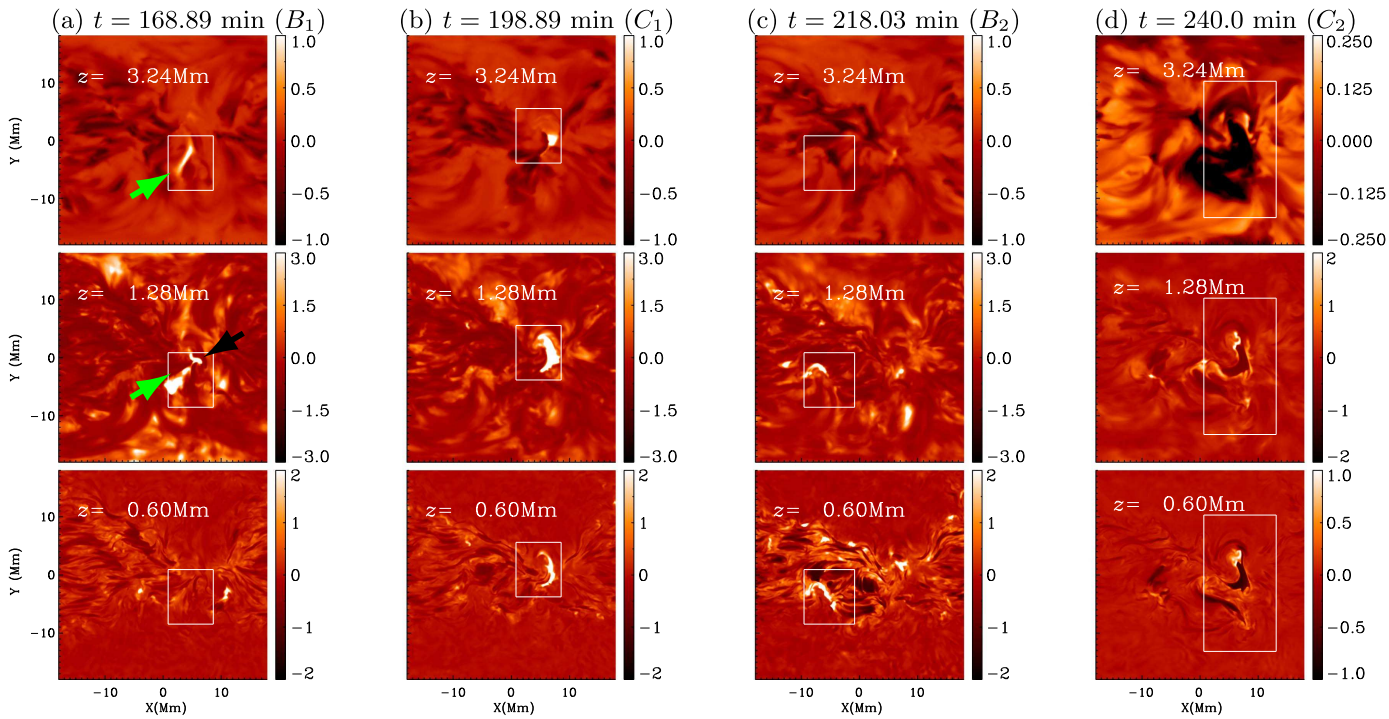

Figure 3. (a) Ratio of the local temperature anomaly, ΔT, to the horizontal average temperature, $\overline{T}(z)$, during the B_1 flare at the three different heights indicated. A value of $\Delta T/\overline{T}(z) = s$ implies that the local temperature is $(s + 1) \times \overline{T}(z)$. The green arrow (top and middle panels) denotes the outward reconnection jet, while the black arrow (middle panel) denotes the hot channel of the magnetic flux rope. (b)–(d) Similar to (a) but for the C_1, B_2, and C_2 flares, respectively. White boxes demarcate the region surrounding the flares. This figure is available as an animation. The animation starts at $t = 112.22$ minutes and ends at 250.72 minutes. The 138.5 minutes of simulation time are compressed into a 45 s animation.

(An animation of this figure is available.)

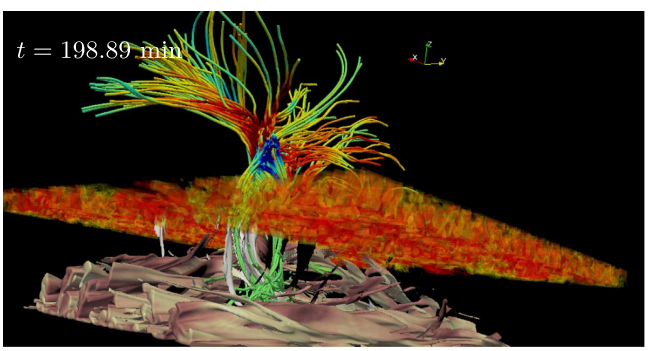

Figure 4. Simulation domain at the time of the C_1 flare. The field lines are colored according to the plasma velocity orientation along them with red (blue) representing upward (downward) velocity.

panels of Figures 5 and 6. The field lines carrying the largest currents appear brighter than the surroundings and can easily be spotted in all of these panels. The regions surrounding these field lines are likely to be hot because of ohmic dissipation. An animation file, qfl.mp4, for the entire simulation duration is provided with the online journal. The epochs of the appearance of bright current-carrying lines in the animation show excellent correlation with the flare onset times calculated using the magnetic energy release (as a function of time) in Chatterjee et al. (2016). The right panels of Figures 5 and 6 depict the quantity $Q_{\rm FL}$ integrated between heights $z_1 = 616$ km and $z_2 = 11.6$ Mm at the snapshot time indicated and can be compared to observational EUV or soft X-ray images of heated coronal loops. Once we have the z-integrated heating $Q_{\rm FL}(x, y)$ at each time, we choose a set of points for each simulation snapshot on the xy-plane where $Q_{\rm FL}(x, y) > Q_c$, a critical value. This critical value has been chosen as 0.5 for flares C_1 and C_2 and 0.125 for B_1 and B_2 so as to obtain a mask of about 500 points for each case. The outer boundary of this masked region is denoted by a red contour in the right panels. In these panels, to show the heated regions clearly, we have zoomed into the region surrounding flares.

In Figure 7, we show the heating function, $\overline{Q}_{\rm FL}(z)$, as a function of z, obtained by averaging $Q_{\rm FL}$ over all points inside the boundary of the red contours shown in the right panels of Figures 5 and 6 for all four flares. Moreover, we have temporally averaged the $\overline{Q}_{\rm FL}$ curves for simulation snapshots between an interval ± 2.8 minutes around the onset time. Just before the onset of any flare, when the function $\overline{Q}_{\rm FL}$ peaks at a certain height, we can conclude that the flare was likely initiated at that height. For flare B_1, the $\overline{Q}_{\rm FL}$ shows a plateau between 0.1 and 2 Mm, whereas for flare B_2, we see a clear peak at 0.5 Mm. Flares C_1 and C_2 also have plateaus between 0.1–3 and 0.1–4 Mm, respectively. Also, the peaks (of $Q_{\rm FL}$) for flares C_1 and C_2 appear at heights 2.6 and 3 Mm above the photosphere, respectively. From these results, and aided by the online animations at corresponding heights—0p55MmFlares.mp4, 1p28MmFlares.mp4, and 3p24MmFlares.mp4—we can conclude that flare B_2 was likely initiated at 0.5 Mm, whereas flares C_1 and C_2 were at $\sim$2.6 and $\sim$3 Mm, respectively. For flare B_1, because of the flat plateau without any pronounced peaks, we can only conclude that it was initiated below a height of 1.5 Mm. The WG_M method will be applied at different heights of the simulation with the goal of understanding its behavior relative to the derived heights of the flare initiation using ohmic heating, as well as temperature signatures. This spatial information, gained from analysis of this simulation,

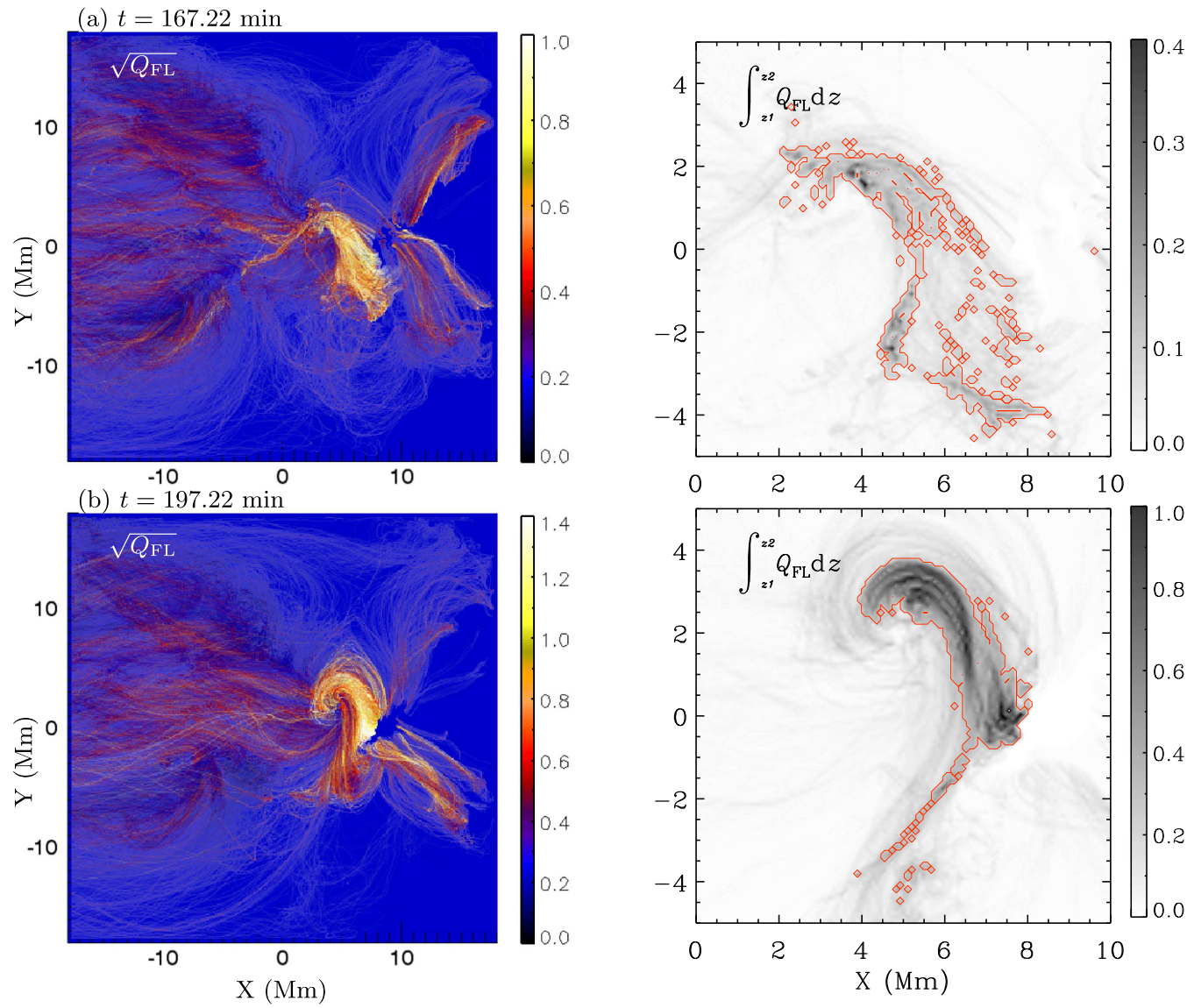

Figure 5. (a) Left panel: square root of the ohmic field line heating, $Q_{\rm FL}$, in arbitrary units at $t = 167.22$ minutes (onset of B_1 flare). Right panel: zoomed-in view of $Q_{\rm FL}$ integrated between heights $z_1 = 616$ km and $z_2 = 11.6$ Mm. The red contour boundary denotes the region where $\int Q_{\rm FL} dz > Q_c (=0.125)$ (see text). (b) Similar to (a) but just before the onset of the C_1 flare and with $Q_c = 0.5$. The left panels are available as an animation. The animation starts at $t = 150.56$ minutes and ends at 255.06 minutes. The 104.5 minutes of simulation time are compressed into a 46 s animation.

(An animation of this figure is available.)

will be compared with the output of the WG_M analysis as a function of height in the next section.

4. Applying the WG_M Method to Simulated Flare Data

4.1. Implementation of the WG_M Method

We investigate the preflare behavior of the simulated 3D δ-type sunspot with the tool put forward by Korsós et al. (2015). Namely, they introduced the weighted horizontal magnetic gradient proxy (denoted as WG_M) between two opposite magnetic polarity umbrae in a δ-spot and demonstrated that the WG_M could be successfully applied to identifying preflare patterns above the M5 energetic flare class. The WG_M proxy is based on two components: (i) the total unsigned magnetic flux summed for all of the considered umbrae of opposite polarities and (ii) the distance between two area-weighted barycenters of positive and negative polarities within the entire δ-spot. Initially, the WG_M method was developed on a sample of 61 cases using the *SOHO*/MDI-Debrecen Data (SDD) and further tested with the SDO/HMI-Debrecen Data (HMIDD, the continuation of the SDD) catalog in Korsós & Ruderman (2016). In empirical analyses, for all of the observed flare cases, two flare precursor patterns were discovered.

1. The preflare behavior of the WG_M quantity itself exhibited characteristic patterns: increase and the maximum value of the magnetic flux gradient followed by a gradual decrease prior to flaring. The aqua inverted V-shape points out the preflare behavior of the WG_M in the top panels of Figures 8–11.
2. The preflare behavior pattern of the distance parameter is based on the approaching–receding motion between the area-weighted barycenters of the positive and negative

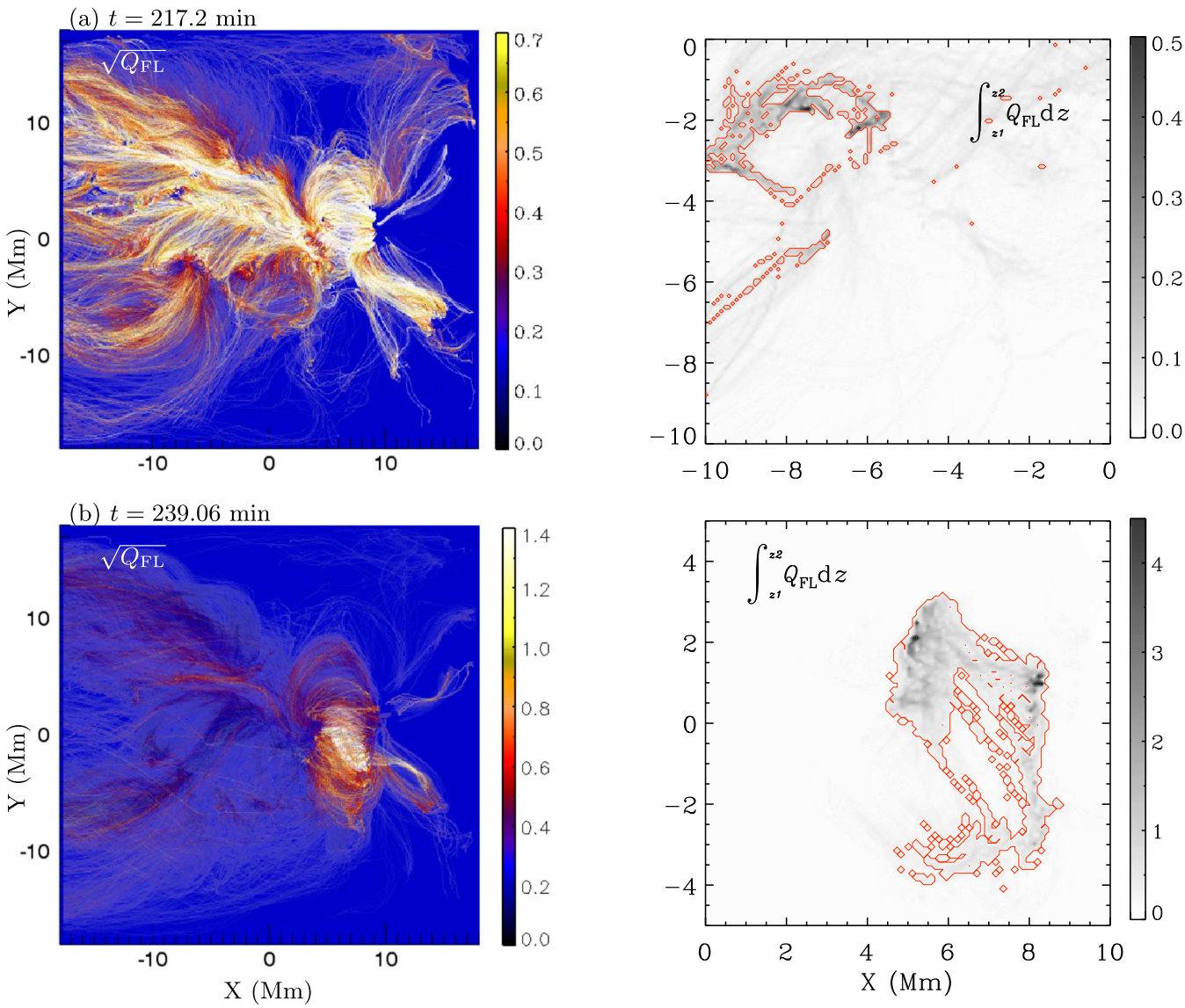

Figure 6. (a) Left panel: square root of the ohmic field line heating, $Q_{\rm FL}$, in arbitrary units at $t = 217.2$ minutes (B_2 flare). Right panel: zoomed-in view of $Q_{\rm FL}$ integrated between heights $z_1 = 616$ km and $z_2 = 11.6$ Mm. The red contour denotes the region where $\int Q_{\rm FL} dz > Q_c (=0.125)$ (see text). (b) Similar to (a) but just before the onset of the C_2 flare and with $Q_c = 0.5$. The left panels are shown in the Figure 5 animation.

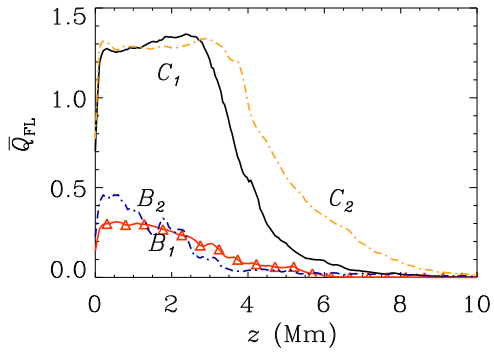

Figure 7. The $\overline{Q}_{\rm FL}$ obtained by integrating the ohmic heating, $Q_{\rm FL}$, over points inside the red boundary marked in Figures 5 and 6 for all four flares.

polarities prior to flare. It was found that the evolution of distance actually has two ways to behave after the moment when the distance has regained the value it had at the beginning of the approaching phase. One way is when the distance is decreasing, and another way is when the distance keeps growing continuously before the flare occurrence. The duration of the approaching–receding motion of the area-weighted barycenters of opposite polarities is highlighted by a red parabolic curve in the middle panels of Figures 8–11. A parabolic curve is fitted from the starting time of the approaching phase to the end of the receding phase, taking its minimum at the moment of reaching the closest position of the two barycenters derived from the minimum point of the data.

In Korsós et al. (2015), the next diagnostic tools were introduced to probe preflare behavior patterns, where the viability of the diagnostic tools was tested on a sample of 61 cases observed during the *SOHO*/MDI era.

1. The first one is based on the relationship between the values of the maxima of the WG_M ($\mathrm{WG}_M^{\max}$) and the highest *GOES* flare intensity class of ARs. In the case of the current, simulated artificial AR, presented here, the

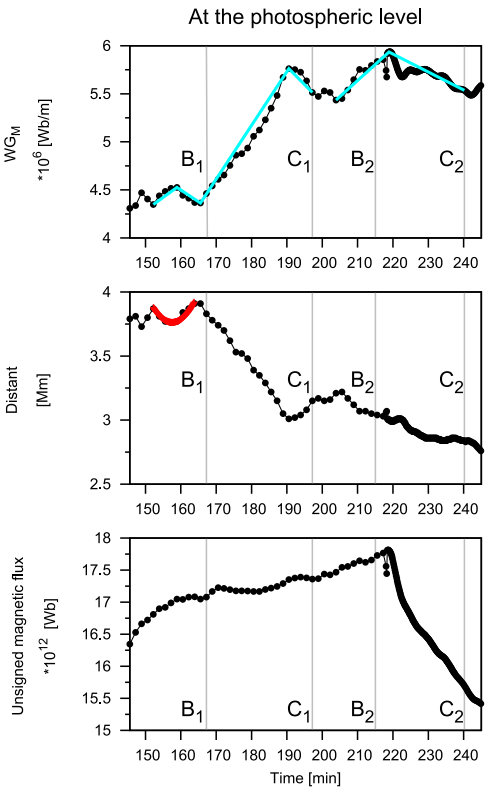

Figure 8. Evolution of various preflare indicators applied to the simulation data. The x-axis is time [minutes]. The top panel shows the temporal variation of the WG_M. The preflare behavior of the WG_M is indicated by the aqua inverted V-shape, where a peak corresponds to a follow-up flare. The middle panel demonstrates the evolution of the distance of the barycenters of opposite polarities. The red curved fit marks the full approaching–receding motion of the distance between area-weighted barycenters of opposite polarities. The vertical gray lines indicate the moments when the flares occurred. Note, however, that the flares do not occur at the photosphere (see, e.g., Figure 7 to determine the height range for the flare location). The bottom panel shows the evolution of the unsigned flux amounts.

applicability of the intensity estimation should be made cautiously, because this relationship has as yet been determined only for high-energy flares, i.e., above M5, while the simulated flares are B and C classes only.

2. Next, the estimation of the flare onset time (T_{est}) is based on the relationship found between the duration of the receding motion of the opposite polarities until the flare onset (T_{D+F}) and the duration of the approaching motion (T_C) of the opposite polarities. K15 also classified the selected spot groups of their study by age—younger or older than 3 days—and repeated the investigation separately for these two groups in order to determine how fundamental this relationship may be. The following regression may be one of the most useful results found from the WG_M method:

$$T_{\mathrm{est}} = a \cdot T_C + b, \tag{3}$$

where $a = 1.29$ (0.85) [hr] and $b = 1.11$ (12.8) [hr] in the younger (older) than 3 day case. Given that the eruptive events in the simulation happen much faster, i.e., on a timescale of minutes rather than hours like in the real Sun due to the practical limiting reasons on CPU access, we need to appropriately rescale the hours-to-minutes

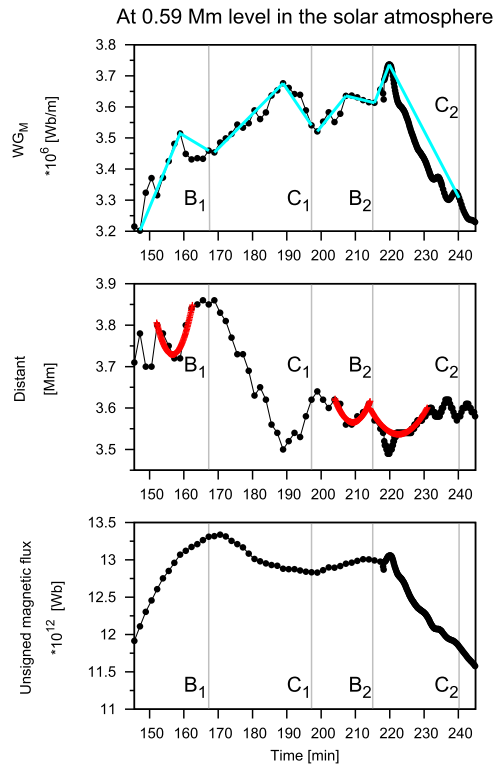

Figure 9. Evolution of the same physical parameters for the artificial AR as in Figure 8, but at the height of 0.59 Mm above the photosphere.

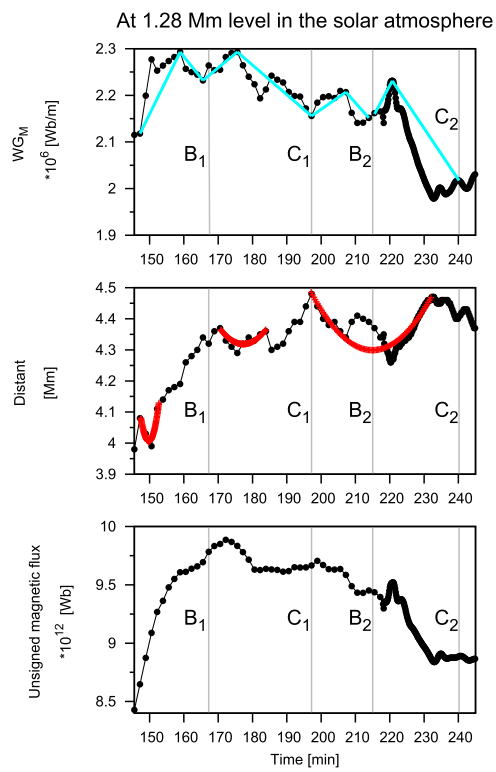

Figure 10. Same as Figure 8, but at the height of 1.28 Mm above the photosphere. Here, the preflare evolution stages of the WG_M for the first two flares are not visible, and there is an indication only for the second C-class flare.

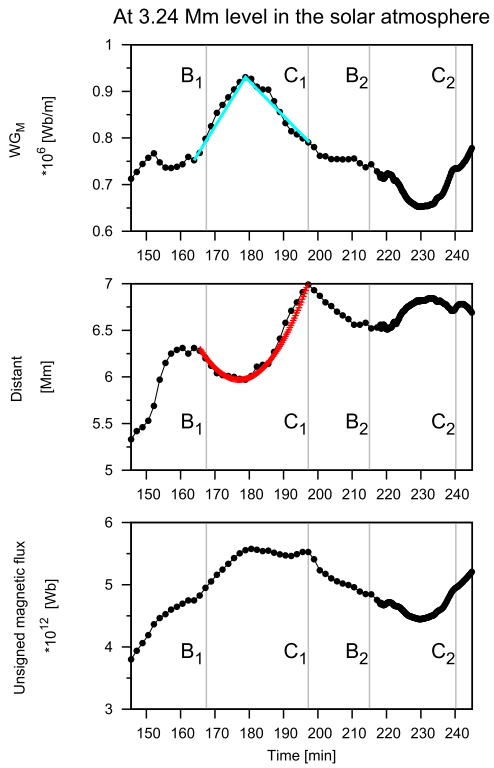

Figure 11. Same as Figure 8, but at 3.24 Mm high in the solar atmosphere. The two B-class flares are only marked for completeness; they cannot be confidently identified.

timescale in Equation (3). Furthermore, we also need to rescale the 3 day (=72 hr) limit of what is labeled younger (older) emerging fluxes to appropriate the minute-scale limit. Now, given the linear structure of Equation (3), we use $a = 1.29$ (0.85) [minutes] and $b = 1.11$ (12.8) [minutes] for the emerging fluxes younger (older) than 72 minutes.

3. The last tool is the percentage difference ($\mathrm{WG}_M^{\%}$) calculated between the values of the preflare $\mathrm{WG}_M^{\max}$ and of the WG_M at the flare moment of onset ($\mathrm{WG}_M^{\mathrm{flare}}$). If $\mathrm{WG}_M^{\%}$ may be over 54%, no further flare of the same class or above would be expected; but, if $\mathrm{WG}_M^{\%}$ is less than ∼42%, further flares of the same class are probable within about an 18 hr window (i.e.,18 minutes in the simulation).

For the preflare behavior of the WG_M and barycentric distance parameters to qualify as a true precursor event and not just fluctuation, it was introduced that the duration of (i) the decrease in the distance parameter during the approaching phase and (ii) the increase in the WG_M has to take place for about at least a minimum of 4 hr for real flares. These conditions were satisfied for over 90% of the studied cases and were accepted as criteria for cutoff to remove fluctuations. Therefore, flux rising or approaching events with shorter durations were considered as fluctuations. Now, given the employed rescaling for the simulation, the applied cutoff here is about 4 minutes. Further, for real solar applications, the δ-spot has to also satisfy to be within a certain belt around the central meridional, i.e., within ±70°; however, this condition is not applicable here, given the chosen geometry providing a perpendicular view representing the solar surface. Finally, and perhaps most importantly, for a precursor event to qualify as a true preflare signature, it is required that events (i) and (ii) must occur concurrently. That is, based on the analysis of the 61 M5 or above flare cases, it was found by K15 that for all of the studied samples, events (i) and (ii) were always present.

4.2. Analysis and Interpretation in Terms of Preflare Dynamics

Let us now apply the WG_M method to the numerically simulated flaring δ-spot. We calculate the WG_M in the entire δ-spot like in the case of real sunspot data. The investigation in terms of the preflare dynamics starts from $t = 145.22$ minutes, i.e., from the moment when the simulated AR finally emerged through the photosphere and developed into a complex set of loops. From the simulation data, e.g., from constructing the temperature contour and $\overline{Q}_{\mathrm{FL}}$ plots at various heights, we know that all of the flares occurred between 0.3 and 3.25 Mm in height (see Figures 3 and 6 for B_1, C_1, B_2, and C_2 flares). These inspire us to extend and apply the flare precursor identification analysis in the solar atmosphere as a function of height, from the photosphere to as high as $z = 3.6$ Mm. The aim is to demonstrate that the flare precursor patterns may appear earlier in time when applied to data available higher in the lower solar atmosphere, as compared to its counterpart form, photospheric analysis.

4.2.1. Investigation of Preflare Behavior at Different Heights

Let us now track the temporal variation of the WG_M, the distance of the area-weighted barycenters of the opposite polarities, and the unsigned magnetic flux at the different heights in the lower solar atmosphere, similar to the analysis carried out earlier with observed data at the photosphere, demonstrated in K15.

At the photosphere. From inspecting Figure 8, we recognize the preflare patterns of the WG_M (aided by the aqua inverted V-shape) as follows: a rising phase and a first maximum value of the flux gradient (at 158.89 minutes, i.e., a peak in the aqua line preceding the first flare) that is followed by a gradual decrease that culminates in the B_1 flare at $t = 167.5$ minutes. About 8 minutes later, after the first maximum value of the WG_M, one finds another (now a much more pronounced) steep rise and the associated high maximum value of the flux gradient (second aqua peak). This peak is followed by a gradual decrease that ends with the C_1 energy flare. Another 10 minutes later, from the C_1 flare, the WG_M again shows a preflare behavior before the C_2 flare (i.e., third aqua peak). Unfortunately, in the case of the B_2 event (for ease and convenience, marked as a gray vertical line), we cannot observe the complete preflare behavior of the WG_M. All that can be said about it is that the B_2 flare happened during the rising phase of the WG_M before the C_2 flare without a precursor signature in the data.

Let us now follow the evolution of the distance parameter in time in the data at the photospheric level (middle panel of Figure 8). We can see the mark of the approaching–receding motion of the area-weighted barycenters of opposite polarities before the B_1 flare (indicated by the red parabola in Figure 8). In the case of subsequent C_1, B_2, and C_2 flares, however, we cannot identify the complete preflare behaviors of the distance parameter using the simulation data available at the photospheric level. For example, after reaching the minimum value during the approaching phase at ∼190 minutes, the value of the distance parameter did not increase enough during the receding phase to regain about the same value as at the start of the

approaching phase, which is a prerequisite for applying the WG_M method successfully.

We conclude at this stage that, using the photospheric data, only the B_1 flare has the required concurrent qualifying precursors for indicating the potential development of a flare. Although there are tempting precursors for the C_1 flare, the distance parameter does show the required full parabolic U shape.

At the 0.59 Mm level in the low chromosphere. In Figure 9, we show the evolution of the three parameters (WG_M, distance, and unsigned magnetic flux) in the low chromosphere. Further, the first point to note is that one more increasing and decreasing phase of the WG_M starts to appear before the B_2 flare, starting from ∼196 minutes. The two additional approaching and receding phases of the distance parameter become identifiable before the B_2 and C_2 flares, respectively. At this level of height, we found (though with some level of fluctuation present) the characteristic increasing and decreasing phase of the WG_M prior to each of these flares (see the aiding aqua lines for marling the four peaks). Also, we observe the signatures of the approaching–receding motion between the area-weighted barycenters of opposite polarities prior to the B_1, B_2, and C_2 flares (marked with three red U shapes).

We conclude at this stage using data at 0.59 Mm that the precursors became more pronounced for the B_1 flare; for B_2, we still cannot be fully certain that a flare may develop, as the distance parameter does not satisfy the minimum 4 minutes' decrease criteria of the U shape. Although there are tempting precursors for the C_1 flare, the distance parameter shows the required full parabolic U shape.

At 1.28 Mm in the middle chromosphere. When one ascends further up in the solar atmosphere and reaches the 1.28 Mm level, one sees changes in the evolution of the WG_M, the distance between area-weighted polarity barycenters, and the unsigned magnetic flux. It is found at this height that the preflare behavior of the WG_M is difficult to recognize prior to the B_1, C_1, B_2, and C_2 flares, but they are there and may qualify as precursors.

In Figure 10, before the C_1 flare, the duration of the approaching–receding motion of the distance starts to form between 170 and 184 minutes, but this interval will become longer in the higher solar atmosphere. The two approaching–receding phases of the distance identified at the 0.59 Mm level (for B_2 and C_2) merge when ascending further to 1.28 Mm. It is also found at this height that the indicator of the approaching–receding motion of the B_1 flare has actually started to disappear. The decrease is only 3.32 minutes before the B_1 flare, which does not satisfy the threshold criterion of a minimum of 4 minutes' decrease.

At 3.24 Mm above the photosphere. As one ascends even higher, one finds that the evolution of the WG_M and distance changes remarkably (see Figure 11) when compared to their behavior at the photosphere (Figure 8). Here we also note that the preflare behavior of the WG_M is recognizable between 145.56 and 161 minutes, which could link to B_1, but we avoid the analysis of B-class flares at this level based on the plateaus of the $\overline{Q}_{FL}$ during flares shown in the simulations (see Figure 7). We also can no longer recognize any meaningful characteristic preflare behaviors of the distance prior to these two small flares.

In the two C-flare cases, when the transition region and the lower corona are reached at this height, we do recognize the following properties of the WG_M and the distance between the area-weighted polarity barycenters. (i) First of all, the steep rise from 164 minutes and a high maximum value of the weighted horizontal gradient of the magnetic field is still followed by a less steep decrease prior to the C_1 flare (see the aqua inverted V-shape). The WG_M only has a rising phase before the C_2 flare at this height. (ii) The approaching and receding characteristic features of the distance prior to the C_1 flare are also there, but the distance parameter does not comply to be a qualifying criterion before the C_2 flare.

Based on the analysis of data available at the very high end of the lower solar atmosphere (i.e., at 3.24 Mm), we conclude that preflare signatures of C_1 can finally be confirmed (as opposed to the cases at lower heights discussed earlier). The signatures of the small B flares are not clear, nor are they for the C_2 flare.

Finally, similar to the observed data of real sunspots, the unsigned magnetic flux (lower panels of Figures 8–11) does not show any special behavior to be useful for the flare precursor.

4.2.2. Optimum Height(s) Search for an Earlier Flare Precursor Identification

The evolution of the WG_M and the distance of the area-weighted barycenters of opposite polarities are different at various heights, as has been described above. In order to improve the flare precursor capability of the WG_M method, therefore, we try to identify optimum height(s) in the solar atmosphere. The investigated heights are where the precursor behaviors of the WG_M and distance parameters are identifiable prior to each flare. The optimum height(s) would be where the distance parameter would yield the earliest sign of preflare behavior in time. Table 2 summarizes the key parameters for finding the optimum heights.

First, in Figure 12, we plot the variation of the start time of the approaching phase (green lines), the moment of the closest approach (blue lines), and the estimated flare onset time (magenta lines) as a function of height. In Figure 12, the filled squares/triangles/circles/stars mark the calculated corresponding data of the $B_1/C_1/B_2/C_2$-class flares. The black vertical lines indicate the onset time of the flares, where the strength of the flare ($B_1/C_1/B_2/C_2$) is labeled on the top axis. The gray regions mark the vertical extent where ohmic heating of the "current-carrying" field lines reaches plateaus of $\overline{Q}_{FL}$ during the flares in the simulations (see Figure 7). Most noticeable is that, in general, there are certain heights above the photosphere where the approaching motions begin and reach the closest point of approach earlier than at the photosphere or at other heights in the solar atmosphere.

In Figure 12, the start time of the approaching phase (first green line with squares) of the B_1 flare is sooner and also reaches the moment of the closest approach sooner (first blue line with squares) between heights at 0.3 and 0.4 Mm than at the photosphere or any other heights. In the case of the B_2 flare, the optimum height, i.e., having the earliest time of beginning of approach, seems to be 0.5 Mm. Similarly, for the C_1 flare, the start time of the approaching phase and the moment of the closest approach are earliest between heights of 2.3 and 2.9 Mm above the photosphere. We can clearly see that the start time of the approaching phase and the moment of closest approach corresponding to the C_2 flare are earliest between heights of 1.2 and 1.8 Mm from the photosphere. This result is rather important: if we are able to identify the optimum height where the moment of the start time of the approaching phase, as well as the moment of closest approach, are indeed earlier than

Table 2
Summary of the Investigated Properties of the Two B- and Two C-class Flares at Their Optimum Heights

Flare	Interval	Optimum Height (Mm)	$\overline{Q}_{\rm FL}$ (Mm)	$\mathrm{WG}_M^{\rm Max}$ $\cdot 10^6$ (Wb m^{-1})	$\mathrm{WG}_M^{\rm flare}$ $\cdot 10^6$ (Wb m^{-1})	T_C (minute)	T_{D+F} (minute)	$T_{\rm est}$ (minute)	$\mathrm{WG}_M^{\%}$ (%)
B_1	Min	0.3	0.1	3.99	3.93	3.34	11.94	5.40	1.5
	Max	0.4	2	3.87	3.80	3.34	11.94	5.40	2
C_1	Min	2.3	0.1	1.36	1.18	11.60	19.98	16.20	13.2
	Max	2.9	3	1.05	0.89	11.60	19.98	16.20	15.2
B_2	Min	0.5	0.5	3.92	3.92	3.34	10	14.7	0.1
	Max								
C_2	Min	1.2	0.1	2.23	2.01	15.70	25.70	25.40	9.5
	Max	1.8	4	1.54	1.39	16.70	24.70	26.2	10

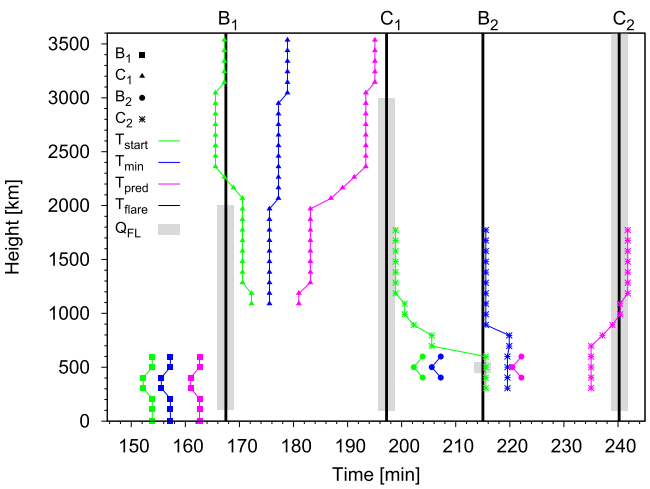

Figure 12. Filled squares/triangles/circles/stars mark $B_1/C_1/B_2/C_2$-class flares, respectively. The actual moment of the start time of the approaching phase (green lines), times of momentum of the closest approaching point between two barycenters (blue lines), and the estimated flare onset time from Equation (3) (magenta lines) are plotted as a function of height. The black vertical lines denote the two B-class and two C-class flares (at 167.5, 215.03, 197.2, and 240.2 minutes). The gray areas demonstrate the height extent where the ohmic heating of their "current-carrying" field lines reach more than 95% of the maximum ($Q_{\rm FL}$) near the onset time of the two B-class and two C-class flares.

at any other heights in the solar atmosphere, then the analysis carried out at this height may (hopefully considerably in practice) improve the capacity of flare precursor capability, e.g., yielding a more accurate flare onset time. Furthermore, it also seems that the optimum height may depend on the energetic flare class. This could be significant progress if confirmed by observations on a larger database.

In Table 2, we list some properties of the flares determined at the minimum and maximum values of their optimum heights and the minimum and maximum height values corresponding to the plateaus of $\overline{Q}_{\rm FL}$. Table 2 includes the maximum value of the WG_M, the value of the WG_M at the flare onset, the duration of the simulated compressing phase (T_C), the receding motion until flare onset (T_{D+F}), the estimated flare onset time ($T_{\rm est}$) elapsed from the moment of reaching the closest point during the approaching–receding motion to the flare (computed from Equation (3)), and the ratio of the maximum value of the WG_M to the value of the WG_M at flare onset. The estimated onset time and the elapsed time of the simulated receding motion until flare onset are close to each other for the two B- and C-class flares at the optimum heights.

First, if we apply T_C obtained from the first approaching–receding motion of the barycentric distances before the B_1 flare between heights of 0.3 and 0.4 Mm, then the time difference is 6.54 minutes between the estimated and simulated flare onset time (see the values in Table 2). The C_1 flare occurred only 3.78 minutes later than the expected onset time. For the B_2 flare, the time difference between the estimated and the observed onset time is a mere 4.7 minutes. The onset time of the C_2 flare is estimated well because it occurred only 1.5 minutes later than one may expect from mere photospheric data. Also, the minimum and maximum values of the optimum heights of the B_1, C_1, B_2, and C_2 flares are in the plateau ranges of $\overline{Q}_{\rm FL}$ (see the values in Table 2).

Last, we investigate the percentage difference ($\mathrm{WG}_M^{\%}$) at identified optimum heights. The $\mathrm{WG}_M^{\%}$ does not seem to be applicable to the simulation data, unlike to observational data. The values of $\mathrm{WG}_M^{\%}$ are small, which means that one may expect further flare(s) during the decreasing phase of the WG_M, but this is not taking place. So, further investigation may be needed to exploit the applicability of this parameter.

5. Conclusion

Chatterjee et al. (2016) modeled a δ-sunspot-like feature formed due to the collision of two magnetic regions with opposite polarity arising from the interaction of emerging magnetic flux with stratified convection. The two opposite polarities of the magnetic field are part of the same initial subsurface structure, and their collision causes recurring flaring.

Four flares were simulated, classified as two B (B_1 and B_2) and two C (C_1 and C_2) classes. To this flaring-simulated AR, we have applied the WG_M method, put forward by Korsós et al. (2015) in the context of identifying flare precursors, and tracked the temporal evolution of the WG_M, the variation of distance between the barycenters of opposite polarities, and the unsigned magnetic flux at different heights in the model solar atmosphere from the photosphere up to 3.6 Mm. We identified two important preflare behaviors at stepping intervals of 100 km in height in the solar atmosphere. (i) Foremost, the typical and characteristic preflare variation of the WG_M was confirmed and found to begin with an increase of its value until a maximum, followed by a decrease until the flare(s) onset. The preflare behavior of the WG_M was found to be height-dependent; at some heights, it was vague and less easy (or impossible) to identify, while at other heights, the behavior was clearly identifiable. The height variation of the clarity of the preflare behavior of the WG_M was also found to be dependent

on the strength of the simulated flare. The B-class energetic flares showed a stronger clarity in terms of the preflare behavior at lower solar atmospheric heights when compared to their counterparts of C-class eruptions. An important common property was also found, namely, the eruption occurred on the decreasing phase of the WG_M in all cases. Therefore, the simulation and application of the WG_M method to the modeled AR is consistent with the preliminary results found when applying this method to real solar data of stronger-than-M5 flares (Korsós et al. 2015). This finding encourages us to suggest that the observational detection of such behavior in the WG_M may serve as a useful and practically simple alert tool for eruption(s) about to occur. (ii) Second, the approaching–receding motion, i.e., the decreasing–increasing distance between the area-weighted polarity barycenters prior to flare (s), seems to be another applicable indicator of an impending flare. Similarly to the preflare behavior of the WG_M, the approaching–receding motion was height-dependent prior to the flares; at some heights, it was vague and less easy to identify, while at other heights, the behavior was clearly identifiable. In general, one may state that the clearest identification was at lower solar atmospheric heights for the B-class flares, while for the C-class flares, it was higher up in the chromosphere.

Next, we investigated the variation of the moment of start time of the approaching phase, the moment of the closest approach, and the estimated flare onset time as a function of height (see Figure 12). This investigation was carried out by searching for specific heights at which the approaching motion of the area-weighted barycenters of the opposite polarities corresponding to a flare event would start earlier and reach its closest approach distance earlier than at any other level (well, at least photospheric level) in the solar atmosphere, so that we may estimate the onset earlier in time. Also, the preflare behavior of the WG_M can be recognized at the optimum heights.

In Figure 12 and Table 2, the start time of the approaching phase and time of closest approach of the area-weighted barycenters of opposite polarities corresponding to the B_1 flare take place earliest between heights of 0.3 and 0.4 Mm than at any other (especially photospheric) level. The estimated onset time ($T_{\rm est}$) of the B_1 flare is 5.4 minutes, according to Equation (3), between 0.3 and 0.4 Mm, compared to the simulated T_{D+F} of 11.94 minutes. In case of the B_2 flare, the optimal height is about 0.5 Mm (i.e., low chromosphere), where the difference is 4.7 minutes between the simulated occurrence time and the estimated onset time. For the C_1 flare, the moment of start time of the approaching phase and moment of reaching the minimum point happened earliest between heights of 2.3 and 2.9 Mm when compared to their photospheric counterparts. From Table 2, we can see that the C_1 flare occurred 3.78 minutes later than the estimated onset time. Furthermore, in Figure 12, we can also see that the moment of start time of the approaching phase of the C_2 flare starts and reaches the closest approach point earlier, at 1.2 Mm measured from the photosphere. Here the onset time for the C_2 flare is well estimated because the flare actually took place only 1.5 minutes later than estimated (see Table 2). The shaded gray areas shown in Figure 12 correspond to the flare initiation height estimates, made using the full width at 95% of the maximum of the ohmic heating curve as defined by $Q_{\rm FL}$ as a function of height. Hence, when comparing the last three rows of Table 1, we find that for all but the B_1 flare, the estimates from all three methods—temperature anomaly (see Figures 3(a)–(d)), ohmic heating peaks (see Figure 7), and the WG_M—agree well with each other. For flare B_1, the temperature anomaly and the Ohmic heating peak location estimates do not agree with the estimate from the WG_M method. We suspect that there may exist a relation between the optimum height for earliest estimation of the flare by the WG_M method and the flare initiation height from the analysis of temperature and Ohmic heating signatures.

In brief summary, we found that the typical preflare dynamics reported in K15 does seem to work for the simulated low-energy flare events, as seen in this case study mimicking the evolution of an AR. Our initial results are encouraging because we do observe very similar preflare behavior of the WG_M and the distance parameter between the polarity barycenters in real sunspot data (K15) as well, indicating that the predictive temporal behavior of these parameters may indeed be an intrinsic feature of the physical processes preceding flare onset. The fact that the application of the WG_M method developed by K15 gives similar results for observed (*GOES* C-, M-, and X-class) flares and simulated (B- and C-class) flares also gives us confidence that a basic physical mechanism of flare initiation has been phenomenologically captured reasonably well in the flare simulation reported in Chatterjee et al. (2016). The other interesting aspect worth mentioning is that the flare precursors are height and flare strength-dependent. Unfortunately, we cannot give a proper physical explanation for this behavior yet, as this would require a more in-depth study of the reconnection process itself that is beyond the scope of the current paper. The height-dependent behavior of the flare precursors may be linked to the so-called push-and-pull reconnection observed in laboratory plasma experiments (Yamada et al. 2010). For a more definite and conclusive statement, one may need to carry out an ensemble of simulations of the evolution of δ-sunspots with flares of higher *GOES* class (M and X classes) and test this relation, as well as the flare precursor capability of the WG_M method, on a statistically significant sample of simulated and observed sunspots.

We thank the anonymous referee for a very careful reading of our manuscript that has led to a marked improvement in the clarity of this paper. M.B.K. is grateful to the University of Sheffield and the Hungarian Academy of Sciences for the support received. M.B.K. also acknowledges the open research program of CAS Key Laboratory of Solar Activity, National Astronomical Observatories, No. KLSA201610. P.C. thanks the University of Sheffield for hospitality and support for a visit during which this work was initiated and the CAS PIFI project 2017VMC0002 and National Astronomical Observatories, Beijing, for support. The simulation was carried out on NASA's Pleiades supercomputer under GID s1061. P.C. also acknowledges computing time awarded on the PARAM Yuva-II supercomputer at C-DAC, India, under the grant name Hydromagnetic-Turbulence-PR. We have used the 3D visualization software Paraview for volume rendering and field line plotting. R.E. is grateful to the Science and Technology Facilities Council (STFC; grant Nos. ST/L006316/1 and ST/M000826/1) UK and the Royal Society for their support. The authors also express their gratitude to Christopher J. Nelson and Michael S. Ruderman (both at

University of Sheffield, UK) for a number of useful discussions and improving the manuscript.

ORCID iDs

M. B. Korsós https://orcid.org/0000-0002-0049-4798
P. Chatterjee https://orcid.org/0000-0002-0181-2495
R. Erdélyi https://orcid.org/0000-0003-3439-4127

References

Archontis, V., & Hood, A. W. 2008, ApJL, 674, L113
Aschwanden, M. J. 2005, Physics of the Solar Corona. An Introduction with Problems and Solutions (2nd ed.; Chichester, UK: Praxis Publishing Ltd.)
Burtseva, O., & Petrie, G. 2013, SoPh, 283, 429
Chatterjee, P., Hansteen, V., & Carlsson, M. 2016, PhRvL, 116, 101101
Cheung, M. C. M., & DeRosa, M. L. 2012, ApJ, 757, 147
DeVore, C. R., & Antiochos, S. K. 2008, ApJ, 680, 740
Evershed, J. 1910, MNRAS, 70, 217
Falconer, D. A., Moore, R. L., & Gary, G. A. 2008, ApJ, 689, 1433
Green, L. M., Kliem, B., & Wallace, A. J. 2011, A&A, 526, A2
Guo, J., Zhang, H., Chumak, O. V., & Liu, Y. 2006, SoPh, 237, 25
Isobe, H., Takasaki, H., & Shibata, K. 2005, ApJ, 632, 1184
Kempf, P. 1910, AN, 185, 197
Korsós, M. B., Ludmány, A., Erdélyi, R., & Baranyi, T. 2015, ApJL, 802, L21
Korsós, M. B., & Ruderman, M. S. 2016, in ASP Conf. Ser. 504, Ground-based Solar Observations in the Space Instrumentation Era, ed. I. Dorotovic, C. E. Fischer, & M. Temmer (San Francisco, CA: ASP), 43
Künzel, H. 1960, AN, 285, 271
Leka, K. D., Canfield, R. C., McClymont, A. N., & van Driel-Gesztelyi, L. 1996, ApJ, 462, 547
Li, J., Mickey, D. L., & LaBonte, B. J. 2005, ApJ, 620, 1092
Livi, S. H. B., Martin, S., Wang, H., & Ai, G. 1989, SoPh, 121, 197
MacTaggart, D., & Hood, A. W. 2009, A&A, 508, 445
Manchester, W., IV, Gombosi, T., DeZeeuw, D., & Fan, Y. 2004, ApJ, 610, 588
Manchester, W., IV, & Low, B. C. 2000, PhPl, 7, 1263
Sammis, I., Tang, F., & Zirin, H. 2000, ApJ, 540, 583
Savcheva, A. S., Green, L. M., van Ballegooijen, A. A., & DeLuca, E. E. 2012, ApJ, 759, 105
Schrijver, C. 2007, ApJL, 655, L117
Selwa, M., Poedts, S., & DeVore, C. R. 2012, ApJL, 747, L21
Shibata, K., & Magara, T. 2011, LRSP, 8, 6
Sterling, A. C., Chifor, C., Mason, H. E., Moore, R. L., & Young, P. R. 2010, A&A, 521, 49
Takizawa, K., & Kitai, R. 2015, SoPh, 290, 2093
van Driel-Gesztelyi, L., Csepura, G., Schmieder, B., Malherbe, J.-M., & Metcalf, T. 1997, SoPh, 172, 151
Wang, J., & Shi, Z. 1993, SoPh, 143, 119
Yamada, M., Kulsrud, R., & Ji, H. 2010, RvMP, 82, 603
Yan, X. L., Qu, Z. Q., & Kong, D. F. 2008, MNRAS, 391, 1887